Abstracta

Ano XXIV - N. 01

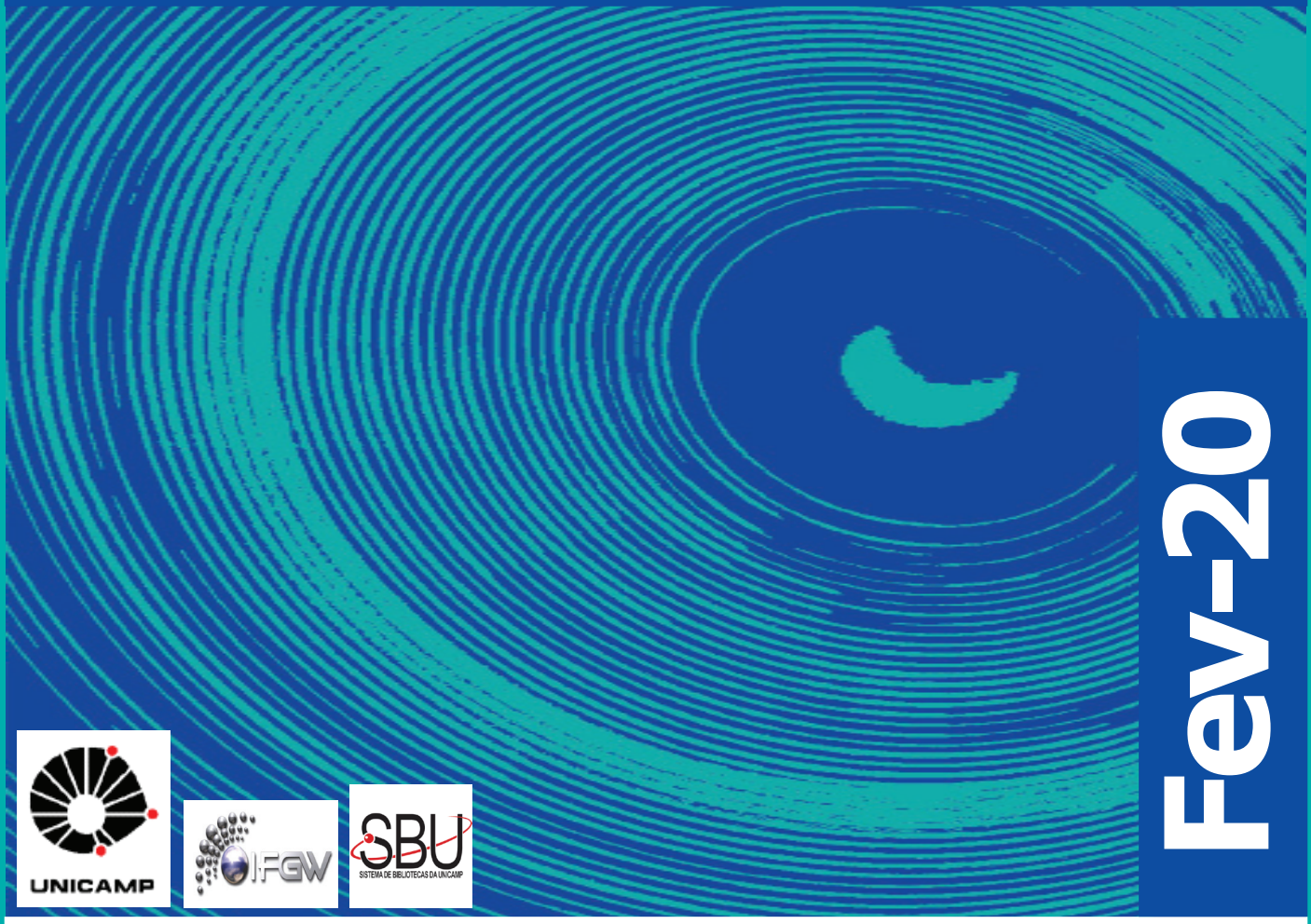

Fev-20

Artigos publicados 2019 - P456-2019 à P495-2019

Eventos publicados 2019 - P496-2019 à P498-2019

Correções 2019 - Co002-2019

Artigos publicados 2020 - P001-2020 à P016-2020

Correções 2020 - Co001-2020

Defesas de Dissertações do IFGW - D001-2020 à D002-2020

Defesas de Teses do IFGW - T001-2020 à T002-2020

Artigos publicados 2019

[P456-2019] "3D-Printed Graphene Electrodes Applied in an Impedimetric Electronic Tongue for Soil Analysis"

da Silva, T. A.*; Braunger, M. L.*; Coutinho, M. A. N.; Amaral, L. R. do; **Rodrigues, V.*; Riul, A. Jr.***

The increasing world population leads to the growing demand for food production without expanding cultivation areas. In this sense, precision agriculture optimizes the production and input usage by employing sensors to locally monitor plant nutrient within agricultural fields. Here, we have used an electronic tongue sensing device based on impedance spectroscopy to recognize distinct soil samples (sandy and clayey) enriched with macronutrients. The e-tongue setup consisted of an array of four sensing units formed by layer-by-layer (LbL) films deposited onto 3D-printed graphene-based interdigitated electrodes (IDEs). The IDEs were fabricated in 20 min using the fused deposition modeling process and commercial polylactic acid-based graphene filaments. The e-tongue comprised one bare and three IDEs functionalized with poly(diallyldimethylammonium chloride) solution/copper phthalocyanine-3,4 ',4 '',4"'-tetrasulfonic acid tetrasodium salt (PDDA/CuTsPc), PDDA/montmorillonite clay (MMt-K), and PDDA/poly(3,4-ethylenedioxythiophene)-poly(styrenesulfonate) (PEDOT:PSS) LbL films. Control samples of sandy and clayey soils were enriched with different concentrations of nitrogen (N), phosphorus (P), and potassium (K) macronutrients. Sixteen soil samples were simply diluted in water and measured using electrical impedance spectroscopy, with data analyzed by principal component analysis. All soil samples were easily distinguished without pre-treatment, indicating the suitability of 3D-printed electrodes in e-tongue analysis to distinguish the chemical fertility of soil samples. Our results encourage further investigations into the development of new tools to support precision agriculture.

CHEMOSENSORS 7[4], 50, 2019. DOI: 10.3390/chemosensors7040050

[P457-2019] "A simulation study of gold nanoparticles localisation effects on radiation enhancement at the mitochondrion scale"

Francis, Z.; Montarou, G.; Incerti, S.; **Bernal, M.***; Zein, S. A.

This paper presents a Monte-Carlo study focusing on the effects of gold nanoparticles on the energy deposition patterns produced by incident photons in the close vicinity of the mitochondrial network modeled as a tube. Spherical shaped gold nanoparticles of 30 nm diameter were placed in a micrometric (10 x 10 x 10 mu m(3)) water phantom containing a tube of 300 nm diameter and 5 mu m length. The tube represented a mitochondrial fragment and nanoparticles were distributed in the water phantom outside the tube. Photons of 120 keV were simulated using the Geant4 Livermore processes and the Geant4-DNA electron processes to account for secondary electrons collisions. The Livermore processes took into account the Auger cascade inside the gold material. A data mining algorithm was then used to analyze the energy deposition clusters inside the water phantom and the tube. A comparison was made between the results obtained for a uniform distribution of nanoparticles and a vesicle distribution model. The results including energy deposition clusters are also compared to dose enhancement ratios.

PHYSICA MEDICA-EUROPEAN JOURNAL OF MEDICAL PHYSICS 67, 148-154, 2019. DOI: 10.1016/j.ejmp.2019.10.038

[P458-2019] "Assessment of phase transition and thermal expansion coefficients by means of secondary multiple reflections of Renninger scans"

dos Santos, A. O.; Lang, R.; Sasaki, J. M.; **Cardoso, L. P.***

This paper reports the successful extension of the basis of the X-ray multiple diffraction phenomenon in the assessment of structural phase transitions and the determination of thermal expansion coefficients along three crystallographic directions, using synchrotron radiation Renninger scans. Suitable simultaneous four-beam cases have accurately resolved the lattice-parameter variation in a nearly perfect single-crystal Rochelle salt using a high-stability temperature apparatus. Secondary reflections observed in the Renninger patterns, chosen by their sensitivity to the shifts in angular position as a function of temperature, have allowed the detection of a monoclinic to orthorhombic phase transition, as well as subtle expansions of all the basic lattice parameters, i.e. without having to carry out measurements on each crystal axis. The thermal expansion coefficients have been estimated from the linear fit of the temperature dependence of the lattice parameters, and are in agreement with those reported in the literature.

JOURNAL OF APPLIED CRYSTALLOGRAPHY 52, 1271-1279, Parte 6, 2019. DOI: 10.1107/S1600576719011944

[P459-2019] "Assessment of Radio-Induced Damage in Endothelial Cells Irradiated with 40 kVp, 220 kVp, and 4 MV X-rays by Means of Micro and Nanodosimetric Calculations"

Tang, N.; Bueno, M.; Meylan, S.; Perrot, Y.; Tran, H. N.; Freneau, A.; Dos Santos, M.; Vaurijoux, A.; Gruel, G.; **Bernal, M. A.*;** Bordage, M. C.; Emfietzoglou, D.; Francis, Z.; Guatelli, S.; Ivanchenko, V.; Karamitros, M.; Kyriakou, I.; Shin, W. G.; Incerti, S.; Villagrasa, C.

The objective of this work was to study the differences in terms of early biological effects that might exist between different X-rays energies by using a mechanistic approach. To this end, radiobiological experiments exposing cell monolayers to three X-ray energies were performed in order to assess the yields of early DNA damage, in particular of double-strand breaks (DSBs). The simulation of these irradiations was set in order to understand the differences in the obtained experimental results. Hence, simulated results in terms of microdosimetric spectra and early DSB induction were analyzed and compared to the experimental data. Human umbilical vein endothelial cells (HUVECs) were irradiated with 40, 220 kVp, and 4 MV X-rays. The Geant4 Monte Carlo simulation toolkit and its extension Geant4-DNA were used for the simulations. Microdosimetric calculations aiming to determine possible differences in the variability of the energy absorbed by the irradiated cell population for those photon spectra were performed on 10,000 endothelial cell nuclei representing a cell monolayer. Nanodosimetric simulations were also carried out using a computation chain that allowed the simulation of physical, physico-chemical, and chemical stages on a single realistic endothelial cell nucleus model including both heterochromatin and euchromatin. DNA damage was scored in terms of yields of prompt DSBs per Gray (Gy) and per giga (10(9)) base pair (Gbp) and DSB complexity was derived in order to be compared to experimental data expressed as numbers of histone variant H2AX (gamma-H2AX) foci per cell. The calculated microdosimetric spread in the irradiated cell population was similar when comparing between 40 and 220 kVp X-rays and higher when comparing with 4 MV X-rays. Simulated yields of induced DSB/Gy/Gbp were found to be equivalent to those for 40 and 220 kVp but larger than those for 4 MV, resulting in a relative biological effectiveness (RBE) of 1.3. Additionally, DSB complexity was similar between the considered photon spectra. Simulated results were in good agreement with experimental data obtained by IRSN (Institut de radioprotection et de surete nucleaire) radiobiologists. Despite differences in photon energy, few differences were observed when comparing between 40 and 220 kVp X-rays in microdosimetric and nanodosimetric calculations.

Nevertheless, variations were observed when comparing between 40/220 kVp and 4 MV X-rays. Thanks to the simulation results, these variations were able to be explained by the differences in the production of secondary electrons with energies below 10 keV.

INTERNATIONAL JOURNAL OF MOLECULAR SCIENCES 20[24]6204, 2019. DOI: 10.3390/ijms20246204

[P460-2019] "Constraints on anomalous HVV couplings from the production of Higgs bosons decaying to tau lepton pairs"

Sirunyan, A. M.; Tumasyan, A.; Adam, W.; **Chinellato, J. A.*; Tonelli Manganote, E. J.***; et. al.; CMS Collaboration

A study is presented of anomalous HVV interactions of the Higgs boson, including its CP properties. The study uses Higgs boson candidates produced mainly in vector boson fusion and gluon fusion that subsequently decay to a pair of tau leptons. The data were recorded by the CMS experiment at the LHC in 2016 at a center-of-mass energy of 13 TeV and correspond to an integrated luminosity of 35.9 fb(-1). A matrix element technique is employed for the analysis of anomalous interactions. The results are combined with those from the H -> 4l decay channel presented earlier, yielding the most stringent constraints on anomalous Higgs boson couplings to electroweak vector bosons expressed as effective cross section fractions and phases: the CP-violating parameter f(a3) cos(phi(a3)) = (0.00 +/- 0.27) x 10(-3) and the CP-conserving parameters f(a2) cos(phi(a2)) = (0.08)(-0.21)(+1.04)) x 10(-3), f(Lambda 1) cos(phi(Lambda 1)) = (0.00)(-0.09)(+0.53)) x 10(-3), and f(Lambda 1)(Z gamma) cos(phi(Z gamma)(Lambda 1)) = (0.0(-1.3)(+1.1)) x 10(-3). The current dataset does not allow for precise constraints on CP properties in the gluon fusion process. The results are consistent with standard model expectations.

PHYSICAL REVIEW D 100[11], 112002, 2019. DOI: 10.1103/PhysRevD.100.112002

[P461-2019] "Dark Energy Survey year 1 results: the relationship between mass and light around cosmic voids"

Fang, Y.; Hamaus, N.; Jain, B.; **Sobreira, F.***; et. al.; DES Collaboration

What are the mass and galaxy profiles of cosmic voids? In this paper, we use two methods to extract voids in the Dark Energy Survey (DES) Year 1 redMaGiC galaxy sample to address this question. We use either 2D slices in projection, or the 3D distribution of galaxies based on photometric redshifts to identify voids. For the mass profile, we measure the tangential shear profiles of background galaxies to infer the excess surface mass density. The signal-to-noise ratio for our lensing measurement ranges between 10.7 and 14.0 for the two void samples. We infer their 3D density profiles by fitting models based on N-body simulations and find good agreement for void radii in the range 15-85 Mpc. Comparison with their galaxy profiles then allows us to test the relation between mass and light at the 10 per cent level, the most stringent test to date. We find very similar shapes for the two profiles, consistent with a linear relationship between mass and light both within and outside the void radius. We validate our analysis with the help of simulated mock catalogues and estimate the impact of photometric redshift uncertainties on the measurement. Our methodology can be used for cosmological applications, including tests of gravity with voids. This is especially promising when the lensing profiles are combined with spectroscopic measurements of void dynamics via redshift-space distortions.

MONTHLY NOTICES OF THE ROYAL ASTRONOMICAL SOCIETY 490[3], 3573-3587, 2019. DOI: 10.1093/mnras/stz2805

[P462-2019] "DarkSide: Latest results and future perspectives"

Bottino, B.; Agnes, P.; Albuquerque, I. F. M.; **Machado, A. A.*; Segreto, E.***; et. al.; DarkSide Collaboration

DarkSide is direct-detection dark-matter experimental project based on radiopure argon. The main goal of the DarkSide program is the detection of rare nuclear elastic collisions with hypothetical dark-matter particles. The present detector, DarkSide-50, placed at Laboratori Nazionali del Gran Sasso (LNCS), is a dual-phase time projection chamber (TPC) filled with ultra-pure liquid argon, extracted from underground sources. Surrounding the TPC to suppress the background there are neutron and muon active vetoes. One of argon key features is the capability to distinguish between electron and nuclear recoils, exploiting the different shapes of the signals. DarkSide-50 new results, obtained using a live-days exposure of 532.4 days, are presented. This analysis sets a 90% C.L. upper limit on the dark matter-nucleon spin-independent cross-section of 1.1 x 10(-4) cm(2) for a WIMP mass of 100 GeV/c(2). The next phase of the project, DarkSide-20k, will be a new detector with a fiducial mass of similar to 20 tons, equipped with cryogenic silicon photomultipliers (SiPM).

NUOVO CIMENTO C-COLLOQUIA AND COMMUNICATIONS IN PHYSICS 42[4], 180, 2019. DOI: 10.1393/ncc/i2019-19180-0

[P463-2019] "Dipole modelling for a robust description of subdiffractional polariton waves"

Feres, F. H.; Barcelos, I. D.; **Mayer, R. A.*;** dos Santos, T. M.; Freitas, R. O.; Raschke, M. B.; Bahamon, D. A.; Maia, F. C. B.

The nanophotonics of van der Waals (vdW) materials relies critically on the electromagnetic properties of polaritons defined on sub-diffraction length scales. Here, we use a full electromagnetic Hertzian dipole antenna (HDA) model to describe the hyperbolic phonon polaritons (HP(2)s) in vdW crystals of hexagonal boron nitride (hBN) on a gold surface. The HP2 waves are investigated by broadband synchrotron infrared nanospectroscopy (SINS) which covers the type I and type II hyperbolic bands simultaneously. Basically, polariton waves, observed by SINS, are assigned to the resultant electric field from the summation over the irradiated electric fields of dipoles distributed along the crystal edge and at the tip location and a non-propagating field. The values of polariton momenta and damping extracted from the HDA model present excellent agreement with theoretical predictions. Our analysis shows that the confinement factor of type I HP(2)s exceeds that of the type II ones by up to a factor of 3. We extract anti-parallel group velocities (v(g)) for type I (v(g,typeI) = -0.005c, c is the light velocity in a vacuum) in relation to type II (v(g,typeII) = 0.05c) polaritonic pulses, with lifetimes of similar to 0.6 ps and similar to 0.3 ps, respectively. Furthermore, by incorporating consolidated optical-near field theory into the HDA model, we simulate real-space images of polaritonic standing waves for hBN crystals of different shapes. This approach reproduces the experiments with a minimal computational cost. Thus, it is demonstrated that the HDA modelling self-consistently explains the measured complex-valued polariton near-field, while being a general approach applicable to other polariton types, like plasmon- and exciton-polaritons, active in the wide range of vdW materials.

NANOSCALE 11[44], 21218-21226, 2019. DOI: 10.1039/c9nr07387f

[P464-2019] "Effect of dimensionality on the optical absorption properties of CsPbI3 perovskite nanocrystals"

Liu, A.; Bonato, L. G.; Sessa, F.; **Almeida, D. B.***; Isele, E.; **Nagamine, G.*; Zagonel, L. F.*;** Nogueira, A. F.; **Padilha, L. A.***; Cundiff, S. T.

The bandgaps of CsPbI3 perovskite nanocrystals are measured by absorption spectroscopy at cryogenic temperatures. Anomalous bandgap kshifts are observed in CsPbI3 nanocubes and nanoplatelets, which are modeled accurately by bandgap renormalization due to lattice vibrational modes. We find that decreasing dimensionality of the CsPbI3 lattice in nanoplatelets greatly reduces electron-phonon coupling, and dominant out-of-plane quantum confinement results in a homogeneously broadened absorption line shape down to cryogenic temperatures. An absorption tail forms at low--temperatures in CsPbI3 nanocubes, which we attribute to shallow defect states positioned near the valence band edge.

JOURNAL OF CHEMICAL PHYSICS 151[19], 191103, 2019. DOI: 10.1063/1.5124399

[P465-2019] "Embedding optical Fiber Bragg Grating (FBG) sensors in 3D printed casings"

Manzo, N. R.; **Callado, G. T.*; Cordeiro, C. M. B.***; Vieira, L. C. M. Jr.

This paper aims to numerical and experimentally study and propose Fiber Bragg Grating (FBG) sensors embedded in 3D printed casings. 3D printed casings offer design freedom, enabling strain measurement of structural systems with complex configuration, and, at low cost due to its easiness to manufacture. The casings were first numerically modeled using a commercial finite element software. After the casing was conceptualized to the user needs, they were printed and introduced in two different applications. Assessing the behavior of 3D printed casings in realistic applications has been explored only by few authors, which is the novelty introduced herein. In both applications, the casings' behavior was analyzed numerical and experimentally. The experimental results were compared with electrical strain gauges. As expected from the numerical analysis results, a calibration factor was determined to accurately predict strain using the embedded FBG sensors. A comprehensive discussion is presented on the topic of calibration factors defined numerical and experimentally.

OPTICAL FIBER TECHNOLOGY 53, 102015, 2019. DOI: 10.1016/j.yofte.2019.102015

[P466-2019] "Equilibrium study of binary mixture biosorption of Cr(III) and Zn(II) by dealginated seaweed waste: investigation of adsorption mechanisms using X-ray photoelectron spectroscopy analysis"

Costa, C. S. D.; Queiroz, B. G. M.; **Landers, R.***; Silva, M. G. C. da; Vieira, M. G. A.

The alginate extraction residue (RES) from the Brazilian Sargassum filipendula was successfully employed as biosorbent in this binary equilibrium study, revealing a greater affinity and selectivity for Cr(III) than for Zn(II). Experimental results also revealed that the process is of endothermic nature and well adjusted by Langmuir-Freundlich binary model. The X-ray photoelectron spectroscopy (XPS) analysis revealed that coordination with hydroxyl groups of RES prevailed in Cr removal, followed by carboxyl-metal complexation. As far as Zn(II) is concerned, ion exchange with carboxylate groups of RES was the largest contributor. Nevertheless, scanning electron microscopy coupled with Fourier transform infrared spectroscopy indicated the participation of sulfate functions in a minor degree.

ENVIRONMENTAL SCIENCE AND POLLUTION RESEARCH 26[28] [SI], 28470-28480, 2019. DOI: 10.1007/s11356-018-2880-7

[P467-2019] "Evolution of Zero-Field Ferrimagnetic Domains and Skyrmions in Exchange-Coupled Pt/CoGd/Pt Confined Nanostructures: Implications for Antiferromagnetic Devices"

Brandao, J.; Dugato, D. A.; **Santos, M. V. P. dos***; Cezar, J. C.

Magnetic skyrmions are small-sized spin textures with nontrivial topology that behave like charged particles under a spin-polarized current. The efficient use of skyrmions on the next generation of technological devices will depend on the controllable creation of sub-100 nm skyrmions, ideally without any external field. We report on the magnetic domains and skyrmions evolution in nanostructured ferrimagnetic Pt/CoGd/Pt multilayers discs at zero magnetic field and room temperature. The tuning of the magnetic structures is studied as a function of the disc size. The ferrimagnetic labyrinthine stripes are succeeded by the formation of multiple or single isolated ferrimagnetic skyrmions depending on the diameter of the disc. Multiple ferrimagnetic skyrmions present an average size of similar to 120 nm, whereas single skyrmions similar to 70 nm. It indicates a strong effect played by the confinement of the disc in modifying the skyrmions density and size. Our results shed light on the single ferrimagnetic skyrmion stability at zero magnetic field, which is a further drive in the realization of antiferromagnetic spintronic devices such as skyrmion-based spin torque nano-oscillators with implications in neuromorphic computing.

ACS APPLIED NANO MATERIALS 2[12], 7532-7539, 2019. DOI: 10.1021/acsanm.9b01593

[P468-2019] "Forward elastic scattering: dynamical gluon mass and semihard interactions"

Broilo, M.; Fagundes, D. A.; Luna, E. G. S.; **Menon, M. J.***

The role of low-x parton dynamics in dictating the high-energy behavior of forward scattering observables at LHC energies is investigated using a QCD-based model with even-under-crossing amplitude dominance at high-energies. We explore the effects of different sets of pre- and post-LHC fine-tuned parton distributions on the forward quantities sigma(tot) and rho, from pp and (p) over barp scattering in the interval 10 GeV-13 TeV. We also investigate the role of the leading soft contribution, the low-energy cuttoff, and the energy dependence of the semihard form factor on these observables. We show that in all cases investigated the highly restrictive data on rho parameter at root s = 13 TeV indicate that a crossing-odd component may play a crucial role in forward elastic scattering at the highest energies, namely the Odderon contribution.

EUROPEAN PHYSICAL JOURNAL C 79[12], 1033, 2019. DOI: 10.1140/epjc/s10052-019-7545-2

[P469-2019] "Highly symmetric random one-dimensional spin models"

Quito, V. L.; Lopes, P. L. S.; Hoyos, Jose A.; **Miranda, E.***

The interplay of disorder and interactions is a challenging topic of condensed matter physics, where correlations are crucial and exotic phases develop. In one spatial dimension, a particularly successful method to analyze such problems is the strong-disorder renormalization group (SDRG). This method, which is asymptotically exact in the limit of large disorder, has been successfully employed in the study of several phases of random magnetic chains. Here we develop an SDRG scheme capable of providing in-depth information on a large class of strongly disordered one-dimensional magnetic chains with a global invariance under a generic continuous group.

Our methodology can be applied to any Lie-algebra valued spin Hamiltonian, in any representation. As examples, we focus on the physically relevant cases of SO(N) and Sp(/V) magnetism, showing the existence of different randomness-dominated phases. These phases display emergent SU(/V) symmetry at low energies and fall into two distinct classes, with meson--like or baryon-like characteristics. Our methodology is here explained in detail and helps to shed light on a general mechanism for symmetry emergence in disordered systems.

PHYSICAL REVIEW B 100[22], 224407, 2019. DOI: 10.1103/PhysRevB.100.224407

[P470-2019] "Limits on point-like sources of ultra-high--energy neutrinos with the Pierre Auger Observatory"

Aab, A.; Abreu, P.; Aglietta, M.; **Chinellato, J. A.*; Daniel, B.*; Diaz Castro, M. L.*; Dobrigkeit, C.*; Fauth, A. C.*; Muller, M. A.*; Pereira, L. A. S.***; et al. Pierre Auger Collaboration

With the Surface Detector array (SD) of the Pierre Auger Observatory we can detect neutrinos with energy between 10(17) eV and 10(20) eV from point-like sources across the sky, from close to the Southern Celestial Pole up to 60 degrees in declination, with peak sensitivities at declinations around similar to -53 degrees and similar to +55 degrees, and an unmatched sensitivity for arrival directions in the Northern hemisphere. A search has been performed for highly-inclined air showers induced by neutrinos of all flavours with no candidate events found in data taken between 1 Jan 2004 and 31 Aug 2018. Upper limits on the neutrino flux from point-like steady sources have been derived as a function of source declination. An unrivaled sensitivity is achieved in searches for transient sources with emission lasting over an hour or less, if they occur within the field of view corresponding to the zenith angle range between 60 degrees and 95 degrees where the SD of the Pierre Auger Observatory is most sensitive to neutrinos.

JOURNAL OF COSMOLOGY AND ASTROPARTICLE PHYSICS [11], 004, 2019. DOI: 10.1088/1475-7516/2019/11/004

[P471-2019] "Mass variance from archival X-ray properties of Dark Energy Survey Year-1 galaxy clusters"

Farahi, A.; Chen, X.; Evrard, A. E.; **Sobreira, F.*;** et. al.; DES Collaboration

Using archival X-ray observations and a lognormal population model, we estimate constraints on the intrinsic scatter in halo mass at fixed optical richness for a galaxy cluster sample identified in Dark Energy Survey Year-One (DES-Y1) data with the redMaPPer algorithm. We examine the scaling behaviour of X--ray temperatures, T-X, with optical richness, lambda(RM), for clusters in the redshift range 0.2 < z < 0.7. X-ray temperatures are obtained from Chandra and XMM observations for 58 and 110 redMaPPer systems, respectively. Despite non-uniform sky coverage, the T-X measurements are > 50 per cent complete for clusters with lambda(RM) > 130. Regression analysis on the two samples produces consistent posterior scaling parameters, from which we derive a combined constraint on the residual scatter, sigma(ln) (T) (vertical bar) (lambda) = 0.275 +/- 0.019. Joined with constraints for T-X scaling with halo mass from the Weighing the Giants program and richness-temperature covariance estimates from the LoCuSS sample, we derive the richness-conditioned scatter in mass, sigma(ln) (M) (vertical bar) (lambda) = 0.30 +/- 0.04((stat)) +/- 0.09((sys)), at an optical richness of approximately 100. Uncertainties in external parameters, particularly the slope and variance of the T-X-mass relation and the covariance of T-X and lambda(RM) at fixed mass, dominate the systematic error. The 95 per cent confidence region from joint sample analysis is relatively broad, sigma(ln) (M) (vertical bar) (lambda) is an element of [0.14, 0.55], or a factor 10 in variance.

MONTHLY NOTICES OF THE ROYAL ASTRONOMICAL SOCIETY 490[3], 3341-3354, 2019. DOI: 10.1093/mnras/stz2689

[P472-2019] "Measurement of the ion fraction and mobility of Po-218 produced in Rn-222 decays in liquid argon"

Agnes, P.; Albuquerque, I. F. M.; Alexander, T.; **Machado, A. A.*; Segreto, E.***; et al.

We report measurements of the charged daughter fraction of Po-218 as a result of the Rn-222 alpha decay, and the mobility of Po-218(+) ions, using radon-polonium coincidences from the U-238 chain identified in 532 live-days of DarkSide-50 WIMP-search data. The fraction of Po-218 that is charged is found to be 0.37 +/- 0.03 and the mobility of Po-218(+) is (8.6 +/- 0.1) x 10(-4) cm(2)/vs.

JOURNAL OF INSTRUMENTATION 14, P11018, 2019. DOI: 10.1088/1748-0221/14/11/P11018

[P473-2019] "Measurements of triple-differential cross sections for inclusive isolated-photon plus jet events in pp collisions at root s=8 TeV"

Sirunyan, A. M.; Tumasyan, A.; Adam, W.; **Chinellato, J. A.*; Tonelli Manganote, E. J.***; et. al.; CMS Collaboration

Measurements are presented of the triple-differential cross section for inclusive isolated-photon+jet events in pp collisions at root s = 8 TeV as a function of photon transverse momentum (p(T)(gamma)), photon pseudorapidity (eta(gamma)), and jet pseudorapidity (eta(jet)). The data correspond to an integrated luminosity of 19.7 fb(-1) that probe a broad range of the available phase space, for vertical bar eta(gamma) vertical bar < 1.44 and 1.57 < vertical bar eta(gamma)vertical bar < 2.50, vertical bar eta(jet)vertical bar < 2.5, 40 < p(T) (gamma) < 1000 GeV, and jet transverse momentum, p(T) (jet), > 25 GeV. The measurements are compared to next--to-leading order perturbative quantum chromodynamics calculations, which reproduce the data within uncertainties.

EUROPEAN PHYSICAL JOURNAL C 79[11], 969, 2019. DOI: 10.1140/epjc/s10052-019-7451-7

[P474-2019] "Multicaloric effect in a multiferroic composite of Gd-5(Si,Ge)(4) microparticles embedded into a ferroelectric PVDF matrix"

Andrade, V. M.*; Amirov, A.; Yusupov, D.; Pimentel, B.; Barroca, N.; Pires, A. L.; Belo, J. H.; Pereira, A. M.; Valente, M. A.; Araujo, J. P.; Reis, M. S.

The coupling between electric, magnetic and elastic features in multiferroic materials is an emerging field in materials science, with important applications on alternative solid-state cooling technologies, energy harvesting and sensors/actuators. In this direction, we developed a thorough investigation of a multiferroic composite, comprising magnetocaloric/magnetostrictive Gd5Si2.4Ge1.6 microparticles blended into a piezo- and pyroelectric poly(vinylidene) fluoride (PVDF) matrix. Using a simple solvent casting technique, the formation and stabilization of PVDF electroactive phases are improved when the filler content increases from 2 to 12 weight fraction (wt.%). This effect greatly contributes to the magnetoelectric (ME) coupling, with the ME coefficient alpha(ME) increasing from 0.3 V/cm.Oe to 2.2 V/cm.Oe, by increasing the amount of magnetic material.

In addition, magnetic measurements revealed that the ME--coupling has influenced the magnetocaloric effect via a contribution from the electroactive polymer and hence leading to a multicaloric effect. These results contribute to the development of multifunctional systems for novel technologies.

SCIENTIFIC REPORTS 9, 18308, 2019. DOI: 10.1038/s41598-019-54635-8

[P475-2019] "New Zero Poisson's Ratio Structures"

Gaal, V.*; Rodrigues, V.*; Dantas, S. O.; **Galvao, D. S.*; Fonseca, A. F.***

Most materials exhibit positive Poisson's ratio (PR) values, but special structures can also present negative and, even rarer, zero (or close to zero) PR. Null PR structures have received much attention due to their unusual properties and potential applications in different fields, such as aeronautics and bioengineering. Herein, a new and simple near-zero PR 2D topological model is presented based on a structural block composed of two smooth and rigid bars connected by a soft membrane or spring. It is not based on reentrant or honeycomb-like configurations, which have been the basis of many null or quasinull PR models. The topological model is 3D printed, and the experimentally obtained PR is -0.003 +/- 0.001 which is one of the closest to zero values ever reported. The possibility to extend this model to 3D systems with compression in any direction is discussed. The advantages and disadvantages of these models are also addressed.

PHYSICA STATUS SOLIDI-RAPID RESEARCH LETTERS 1900564, 2019. DOI: 10.1002/pssr.201900564

[P476-2019] "Nonequilibrium path-ensemble averages for symmetric protocols"

Nguyen, T. H.; Ngo, V.; **Zerba, J. P. C.***; Noskov, S.; Minh, D. D. L.

According to the nonequilibrium work relations, path-ensembles generated by irreversible processes in which a system is driven out of equilibrium according to a predetermined protocol may be used to compute equilibrium free energy differences and expectation values. Estimation has previously been improved by considering data collected from the reverse process, which starts in equilibrium in the final thermodynamic state of the forward process and is driven according to the time-reversed protocol. Here, we develop a theoretically rigorous statistical estimator for nonequilibrium path-ensemble averages specialized for symmetric protocols, in which forward and reverse processes are identical. The estimator is tested with a number of model systems: a symmetric 1D potential, an asymmetric 1D potential, the unfolding of deca-alanine, separating a host--guest system, and translocating a potassium ion through a gramicidin A ion channel. When reconstructing free energies using data from symmetric protocols, the new estimator outperforms existing rigorous unidirectional and bidirectional estimators, converging more quickly and resulting in a smaller error. However, in most cases, using the bidirectional estimator with data from a forward and reverse pair of asymmetric protocols outperforms the corresponding symmetric protocol and estimator with the same amount of simulation time. Hence, the new estimator is only recommended when the bidirectional estimator is not feasible or is expected to perform poorly. The symmetric estimator shows similar performance to a unidirectional protocol of half the length and twice the number of trajectories.

JOURNAL OF CHEMICAL PHYSICS 151[19], 194103, 2019. DOI: 10.1063/1.5121306

[P477-2019] "Piezo-optomechanical coupling of a 3D microwave resonator to a bulk acoustic wave crystalline resonator"

Carvalho, N. C.*; Bourhill, J.; Goryachev, M.; Galliou, S.; Tobar, M. E.

We report the observation of coupling between a 3D microwave cavity mode and a bulk mechanical resonator mediated by piezoelectric and radiation pressure effects. The system is composed of a quartz bulk acoustic wave resonator placed inside a microwave re-entrant cavity, which is designed to act as both the electrodes for piezoelectric actuation and a 3D resonator. The cavity electromagnetic mode is modulated by a 5 MHz bulk acoustic wave shear mode, which is modeled and experimentally verified using the input-output formalism. Through finite element method simulations, we calculate the various contributions to the electromechanical coupling and discuss the potential of the system to reach high cooperativities as well as suitable applications.

APPLIED PHYSICS LETTERS 115[21], 211102, 2019. DOI: 10.1063/1.5127997

[P478-2019] "Probing the chiral magnetic wave in pPb and PbPb collisions at root S-NN=5.02 TeV using charge-dependent azimuthal anisotropies"

Sirunyan, A. M.; Tumasyan, A.; Adam, W.; **Chinellato, J. A.*; Tonelli Manganote, E. J.***; et. al.; CMS Collaboration

Charge-dependent anisotropy Fourier coefficients (v(n)) of particle azimuthal distributions are measured in pPb and PbPb collisions at root S-NN = 5.02 TeV with the CMS detector at the LHC. The normalized difference in the second-order anisotropy coefficients (v(2)) between positively and negatively charged particles is found to depend linearly on the observed event charge asymmetry with comparable slopes for both pPb and PbPb collisions over a wide range of charged particle multiplicity. In PbPb, the third-order anisotropy coefficient v(3) shows a similar linear dependence with the same slope as seen for v(2). The observed similarities between the v(2) slopes for pPb and PbPb, as well as the similar slopes for v(2) and v(3) in PbPb, are compatible with expectations based on local charge conservation in the decay of clusters or resonances, and constitute a challenge to the hypothesis that, at LHC energies, the observed charge asymmetry dependence of v(2) in heavy ion collisions arises from a chiral magnetic wave.

PHYSICAL REVIEW C 100[6], 064908, 2019. DOI: 10.1103/PhysRevC.100.064908

[P479-2019] "Probing the origin of ultra-high-energy cosmic rays with neutrinos in the EeV energy range using the Pierre Auger Observatory"

Aab, A.; Abreu, P.; Aglietta, M.; **Chinellato, J. A.*; Daniel, B.*; Castro, M. L. Diaz*; Dobrigkeit, C.*; Fauth, A. C.*; Muller, M. A.*; Pereira, L. A. S.***; et. al.; Pierre Auger Collaboration

Neutrinos with energies above 10(17) eV are detectable with the Surface Detector Array of the Pierre Auger Observatory. The identification is efficiently performed for neutrinos of all flavors interacting in the atmosphere at large zenith angles, as well as for Earth-skimming tau neutrinos with nearly tangential trajectories relative to the Earth. No neutrino candidates were found in similar to 14.7 years of data taken up to 31 August 2018. This leads to restrictive upper bounds on their flux. The 90% C.L. single-flavor limit to the diffuse flux of ultra-high-energy neutrinos with an E-nu(-2) spectrum in the energy range 1.0 x 10(17) eV-2.5 x 10(19) eV is E(2)dN(nu)/dE(nu) < 4.4 x 10(-9) GeV cm(-2) s(-1) sr(-1),

placing strong constraints on several models of neutrino production at EeV energies and on the properties of the sources of ultra-high-energy cosmic rays.

JOURNAL OF COSMOLOGY AND ASTROPARTICLE PHYSICS 10,022, 2019. DOI: 10.1088/1475-7516/2019/10/022

[P480-2019] "Proton-proton forward scattering at the LHC"

Broilo, M.; Fagundes, D. A.; Luna, E. G. S.; **Menon, M. J.***

Recently the TOTEM experiment at the LHC has released measurements root 2 = 13 TeV of the proton-proton total cross section, sigma(tot), and the ratio of the real to imaginary parts of the forward elastic amplitude, rho. Since then an intense debate on the C-parity asymptotic nature of the scattering amplitude was initiated. We examine the proton-proton and the antiproton-proton forward data above 10 GeV in the context of an eikonal QCD-based model, where nonperturbative effects are readily included via a QCD effective charge. We show that, despite an overall satisfactory description of the forward data is obtained by a model in which the scattering amplitude is dominated by only crossing-even elastic terms, there is evidence that the introduction of a crossing-odd term may improve the agreement with the measurements of rho at root 2 = 13 TeV. In the Regge language the dominant even(odd)--under-crossing object is the so called Pomeron (Odderon).

PHYSICS LETTERS B 799, 135047, 2019. DOI: 10.1016/j.physletb.2019.135047

[P481-2019] "Pseudorapidity distributions of charged hadrons in xenon-xenon collisions at root S-NN=5.44 TeV"

Sirunyan, A. M.; Tumasyan, A.; Adam, W.; **Chinellato, J. A.*; Tonelli Manganote, E. J.***; et. al.; CMS Collaboration

Measurements of the pseudorapidity distributions of charged hadrons produced in xenon-xenon collisions at a nucleon--nucleon centre-of-mass energy of root S-NN = 5.44 TeV are presented. The measurements are based on data collected by the CMS experiment at the LHC. The yield of primary charged hadrons produced in xenon-xenon collisions in the pseudorapidity range vertical bar eta vertical bar < 3.2 is determined using the silicon pixel detector in the CMS tracking system. For the 5% most central collisions, the chargedhadron pseudorapidity density in the midrapidity region vertical bar eta vertical bar < 0.5 is found to be 1 187 +/- 36 (syst), with a negligible statistical uncertainty. The rapidity distribution of charged hadrons is also presented in the range vertical bar y vertical bar < 3.2 and is found to be independent of rapidity around y = 0. Existing Monte-Carlo event generators are unable to simultaneously describe both results. Comparisons of charged-hadron multiplicities between xenon-xenon and lead-lead collisions at similar collision energies show that particle production at midrapidity is strongly dependent on the collision geometry in addition to the system size and collision energy.

PHYSICS LETTERS B 799, 135049, 2019. DOI: 10.1016/j.physletb.2019.135049

[P482-2019] "Reprint of "Evidence for color dichotomy in the primordial Neptunian Trojan population"

Lin, Hsing Wen; Gerdes, David W.; Hamilton, Stephanie J.; **Sobreira, F.***; et. al.

In the current model of early Solar System evolution, the stable members of the Jovian and Neptunian Trojan populations were captured into resonance from the leftover reservoir of planetesimals during the outward migration of the giant planets. As a result, both Jovian and Neptunian Trojans share a common origin with the primordial disk population, whose other surviving members constitute today's trans-Neptunian object (TNO) populations. The cold (low inclination and small eccentricity) classical TNOs are ultra -red, while the dynamically excited "hot" (high inclination and larger eccentricity) population of TNOs contains a mixture of ultra-red and blue objects. In contrast, Jovian and Neptunian Trojans are observed to be blue. While the absence of ultra-red Jovian Trojans can be readily explained by the sublimation of volatile material from their surfaces due to the high flux of solar radiation at 5 AU, the lack of ultra -red Neptunian Trojans presents both a puzzle and a challenge to formation models. In this work we report the discovery by the Dark Energy Survey (DES) of two new dynamically stable L4 Neptunian Trojans, 2013 VX30 and 2014 UU240, both with inclinations i > 30, making them the highest-inclination known stable Neptunian Trojans. We have measured the colors of these and three other dynamically stable Neptunian Trojans previously observed by DES, and find that 2013 VX30 is ultra -red, the first such Neptunian Trojan in its class. As such, 2013 VX30 may be a "missing link" between the Trojan and TNO populations. Using a simulation of the DES TNO detection efficiency, we find that there are 162 +/- 73 Trojans with H-r < 10 at the L4 Lagrange point of Neptune. Moreover, the blue-to -red Neptunian Trojan population ratio should be higher than 17:1. Based on this result, we discuss the possible origin of the ultra -red Neptunian Trojan population and its implications for the formation history of Neptunian Trojans.

ICARUS 334, 79-88, 2019. DOI: 10.1016/j.icarus.2019.113433

[P483-2019] "Reusable polymer optics fiber strain sensor with memory capability based on ABS crazing"

Cabral, T. D.*; da Silva, L. E.*; Fujiwara, E.; Ng, A. K. L; Ebendorff-Heidepriem, H.; **Cordeiro, C. M. B.***

A reusable memory capable polymer optical fiber (POF) strain sensor is reported. The fiber consists of an acrylonitrite butadiene styrene (ABS) core and polymethylmethacrylate cladding. The memory capability is derived from stress whitening due to crazing of the ABS core, which can be reversed by heating the fiber close to the ABS glass transition temperature. The probe was characterized under transverse compressive load, macrobending, and tensile loading. Testing shows that the optical properties of the fiber can be reversed to near pristine ABS conditions after thermal recovery and that the POF can be used on the accurate assessment of indentation, flexural and tensile loading, static or cyclical, even after removal of the load. The reusability of the proposed sensor combined with a deeper understanding of the memory mechanisms in POFs are of great interest for the development of new large-strain sensors for modern applications.

APPLIED OPTICS 58[36], 9870-9875, 2019. DOI: 10.1364/AO.58.009870

[P484-2019] "Search for long-lived particles using delayed photons in proton-proton collisions at root s=13 TeV"

Sirunyan, A. M.; Tumasyan, A.; Adam, W.; **Chinellato, J. A.*; Tonelli Manganote, E. J.***; et. al.; CMS Collaboration

A search for long-lived particles decaying to photons and weakly interacting particles, using protonproton collision data at root s = 13 TeV collected by the CMS experiment in 2016-2017 is presented. The data set corresponds to an integrated luminosity of 77.4 fb(-1). Results are interpreted in the context of supersymmetry with gauge-mediated supersymmetry breaking, where the neutralino is long-lived and decays to a photon and a gravitino.

Limits are presented as a function of the neutralino proper decay length and mass. For neutralino proper decay lengths of 0.1, 1, 10, and 100 m, masses up to 320, 525, 360, and 215 GeV are excluded at 95% confidence level, respectively. We extend the previous best limits in the neutralino proper decay length by up to one order of magnitude, and in the neutralino mass by up to 100 GeV.

PHYSICAL REVIEW D 100[11], 112003, 2019. DOI: 10.1103/PhysRevD.100.112003

[P485-2019] "Search for low mass vector resonances decaying into quark-antiquark pairs in proton-proton collisions at root s=13 Tev"

Sirunyan, A. M.; Tumasyan, A.; Adam, W.; **Chinellato, J. A.*; Tonelli Manganote, E. J.***; et. al.; CMS Collaboration

A search for low mass narrow vector resonances decaying into quark-antiquark pairs is presented. The analysis is based on data collected in 2017 with the CMS detector at the LHC in proton-proton collisions at a center-of-mass energy of 13 TeV, corresponding to an integrated luminosity of 41.1 fb(-1). The results of this analysis are combined with those of an earlier analysis based on data collected at the same collision energy in 2016, corresponding to 35.9 fb(-1). Signal candidates will be recoiling against initial state radiation and are identified as energetic, large-radius jets with two pronged substructure. The invariant jet mass spectrum is probed for a potential narrow peaking signal over a smoothly falling background. No evidence for such resonances is observed within the mass range of 50-450 GeV. Upper limits at the 95% confidence level are set on the coupling of narrow resonances to quarks, as a function of the resonance mass. For masses between 50 and 300 GeV these are the most sensitive limits to date. This analysis extends the earlier search to a mass range of 300-450 GeV, which is probed for the first time with jet substructure techniques.

PHYSICAL REVIEW D 100[11], 112007, 2019. DOI: 10.1103/PhysRevD.100.112007

[P486-2019] "Search for Low-Mass Quark-Antiquark Resonances Produced in Association with a Photon at root s=13 TeV"

Sirunyan, A. M.; Tumasyan, A.; Adam, W.; **Chinellato, J. A.*; Tonelli Manganote, E. J.***; et. al.; CMS Collaboration

A search for narrow low-mass resonances decaying to quark--antiquark pairs is presented. The search is based on proton--proton collision events collected at 13 TeV by the CMS detector at the CERN LHC. The data sample corresponds to an integrated luminosity of 35.9 fb(-1), recorded in 2016. The search considers the case where the resonance has high transverse momentum due to initial-state radiation of a hard photon. To study this process, the decay products of the resonance are reconstructed as a single large-radius jet with two-pronged substructure. The signal would be identified as a localized excess in the jet invariant mass spectrum. No evidence for such a resonance is observed in the mass range 10 to 125 GeV. Upper limits at the 95% confidence level are set on the coupling strength of resonances decaying to quark pairs. The results obtained with this photon trigger strategy provide the first direct constraints on quark-antiquark resonance masses below 50 GeV obtained at a hadron collider.

PHYSICAL REVIEW LETTERS 123[23], 231803, 2019. DOI: 10.1103/PhysRevLett.123.231803

[P487-2019] "Search for Physics beyond the Standard Model in Events with Overlapping Photons and Jets"

Sirunyan, A. M.; Tumasyan, A.; Adam, W.; **Chinellato, J. A.*; Tonelli Manganote, E. J.***; et. al.; CMS Collaboration

Results are reported from a search for new particles that decay into a photon and two gluons, in events with jets. Novel jet substructure techniques are developed that allow photons to be identified in an environment densely populated with hadrons. The analyzed proton-proton collision data were collected by the CMS experiment at the LHC, in 2016 at root s = 13 TeV, and correspond to an integrated luminosity of 35.9 fb(-1). The spectra of total transverse hadronic energy of candidate events are examined for deviations from the standard model predictions. No statistically significant excess is observed over the expected background. The first cross section limits on new physics processes resulting in such events are set. The results are interpreted as upper limits on the rate of gluino pair production, utilizing a simplified stealth supersymmetry model. The excluded gluino masses extend up to 1.7 TeV, for a neutralino mass of 200 GeV and exceed previous mass constraints set by analyses targeting events with isolated photons.

PHYSICAL REVIEW LETTERS 123[24], 241801, 2019. DOI: 10.1103/PhysRevLett.123.241801

[P488-2019] "Significant coercivity enhancement at low temperatures in magnetically oriented cobalt ferrite nanoparticles"

Tancredi, P.; Rivas-Rojas, P. C.; Moscoso-Londono, O.; **Muraca, D.*; Knobel, M.***; Socolovsky, L. M.

The present work describes a synthesis and characterization strategy employed to study the magnetic anisotropic properties of a diluted nanoparticulate system. The system under analysis is composed of monodisperse and highly crystalline 16 nm Co0.5Fe2.5O4 nanoparticles (NPs), homogenously dispersed in 1-octadecene. Owing to the liquid nature of the matrix at room temperature, the relative orientation of the nanoparticle easy axis can be controlled by an external magnetic field, enabling us to measure how the magnetic properties are modified by the alignment of the particles within the sample. In turn, by employing this strategy, we have found a significant hardness and squareness enhancement of the hysteresis loop in the magnetically oriented system, with the coercive field reaching a value as high as 30.2 kOe at low temperatures. In addition, the magnetic behavior associated with the system under study was supported by additional magnetic measurements, which were ascribed to different events expected to take place throughout the sample characterization, such as the melting process of the 1-octadecene matrix or the NP relaxation under the Brownian mechanism at high temperatures.

APPLIED PHYSICS LETTERS 115[26], 263104, 2019. DOI: 10.1063/1.5131259

[P489-2019] "Structural, Dielectric, and Magnetic Properties of Multiferroic (1-x) La0.5Ca0.5MnO3-(x) BaTi0.8Sn0.2O3 Laminated Composites"

Ben Moumen, S.; Gagou, Y.; Belkhadir, S.; Mezzane, D.; Amjoud, M.; Rozic, B.; Hajji, L.; Kutnjak, Z.; Jaglicic, Z.; Jagodic, M.; El Marssi, M.; **Kopelevich, Y.***; Luk'yanchuk, Igor A.

High-performance lead-free multiferroic composites are desired to replace the lead-based ceramics in multifunctional device applications. Laminated compounds were prepared from ferroelectric and ferromagnetic materials. In this work, we present the laminated ceramics compound by considering the ferromagnetic La0.5Ca0.5MnO3 (LCMO) and the ferroelectric BaTi0.8Sn0.2O3 (BTSO) in two different proportions.

Compounds (1 - x) LCMO-(x) BTSO with x = 1 and 0 (pure materials) were synthesized by the sol-gel method, and x = 0.7 and 0.5 (laminated) compounds were elaborated by welding appropriate mass ratios of each pure material by using the silver paste technique. Structural, dielectric, ferroelectric, microstructure, and magnetic characterizations were conducted on these samples. X-ray scattering results showed pure perovskite phases confirming the successful formation of both LCMO and BTSO. Scanning electron microscope (SEM) images evidenced the laminated structure and good quality of the interfaces. The laminated composite materials have demonstrated a multiferroic behavior characterized by the ferroelectric and the ferromagnetic hysteresis loops. Furthermore, the enhancement of the dielectric constant in the laminated composite samples is mainly attributed to the Maxwell-Wagner polarization.

IEEE TRANSACTIONS ON ULTRASONICS FERROELECTRICS AND FREQUENCY CONTROL 66[12], 1935-1941, 2019. DOI: 10.1109/TUFFC.2019.2935459

[P490-2019] "The 3HSP catalogue of extreme and high-synchrotron peaked blazars"

Chang, Y. -L.; **Arsioli, B.***; Giommi, P.; Padovani, P.; Brandt, C. H.

Aims. High-synchrotron peaked blazars (HSPs or HBLs) play a central role in very high-energy (VHE) gamma-ray astronomy, and likely in neutrino astronomy. Currently, the largest compilation of HSP blazars, the 2WHSP sample, includes 1691 sources, but it is not complete in the radio or in the X-ray band. In order to provide a larger and more accurate set of HSP blazars that is useful for future statistical studies and to plan for VHE/TeV observations, we present the 3HSP catalogue, the largest sample of extreme and high-synchrotron peaked (EHSP; HSP) blazars and blazar candidates. Methods. We implemented several ways to improve the size and the completeness of the 2WHSP catalogue and reduced the selection biases to be taken into consideration in population studies. By discarding the IR constraint and relaxing the radio-IR and IR-X-ray slope criteria, we were able to select more sources with nu(peak) close to the 10(15) Hz threshold and objects where the host galaxy dominates the flux. The selection of extra sources now commences with a cross-matching between radio and X-ray surveys, applying a simple flux ratio cut. We also considered Fermi-LAT catalogues to find reasonable HSP-candidates that are detected in the gamma-ray band but are not included in X-ray or radio source catalogues. The new method, and the use of newly available multi-frequency data, allowed us to add 395 sources to the sample, to remove 73 2WHSP sources that were previously flagged as uncertain and could not be confirmed as genuine HSP blazars, and to update parameters obtained by fitting the synchrotron component. Results. The 3HSP catalogue includes 2013 sources, 88% of which with a redshift estimation, a much higher percentage than in any other list of HSP blazars. All new gamma-ray detections are described in the First and Second Brazil ICRANet gamma-ray blazar catalogues (1BIGB & 2BIGB) also taking into account the 4FGL list of gamma-ray sources published by the Fermi Large Area Telescope (Fermi-LAT) team. Moreover, the cross-matching between the 2WHSP, 2FHL HSP, and IceCube neutrino positions suggests that HSPs are likely counterparts of neutrino events, which implies the 3HSP catalogue is also useful in that respect. The 3HSP catalogue shows improved completeness compared to its predecessors, the 1WHSP and 2WHSP catalogues, and follows the track of their increasing relevance for VHE astronomy.

ASTRONOMY & ASTROPHYSICS 632, A77, 2019. DOI: 10.1051/0004-6361/201834526

[P491-2019] "The influence of magnetic field geometry in neutron stars' crustal oscillations"

de Souza, G. H.*; Kemp, E.*

In this work, we have studied oscillations in the crust of a neutron star whose magnetic field has both dipolar and toroidal components; the former extends from the stellar interior to the outer space, and the latter is confined inside the star radius. Our study is based on the solutions we have obtained for perturbations in the star fluid, confined to the crust thickness. Our results are compared to the frequencies observed in the soft gamma repeaters signals.

ASTRONOMISCHE NACHRICHTEN 340[9-10], 2019. DOI: 10.1002/asna.201913715

[P492-2019] "Thermal and nonlinear optical properties of Tm3+-doped tellurite glasses"

Seshadri, M.; Radha, M.; Darabian, H.; **Barbosa, L. C.***; Bell, M. J. V.; Anjos, V.

In the present work, thermal and nonlinear properties of tellurite glasses doped with Tm2O3 were investigated by means of thermal lens, thermal relaxation and z-scan measurements. The composition of the samples was (78 - x) TeO2 + 4.5 Bi2O3 + 5.5 ZnO + 10.5 Li2O + 1.5 Nb2O5 + xTm(2)O(3) (x = 0.05, 0.1, 0.5, 1.0 and 1.5 mol%). Thermal diffusivity (D), specific heat (rho c), thermal conductivity (K) and optical path change with temperature (ds/dT) were determined as a function of Tm3+ concentration. Concerning thermal-optical properties, our results show that the 0.5 mol% Tm doped is the most suitable sample for laser applications as it presented the lowest ds/dT and highest thermal diffusivity (conductivity). Third-order nonlinearities were observed and discussed in 1.0 and 1.5 mol% samples. The nonlinear indices (n(2)) found were 1.16 x 10(-13) and 3.89 x 10(-13) cm(2) W-1, respectively. The data obtained show that the Tm3+-doped TBZLN glasses have potential for future opto-electronic devices.

JOURNAL OF THERMAL ANALYSIS AND CALORIMETRY 138[5], 2971-2978, 2019. DOI: 10.1007/s10973-019-08344-z

[P493-2019] "Thermoplasmonic Maskless Lithography on Upconverting Nanocomposites Assisted by Gold Nanostars"

Martinez, E. D.*; Urbano, R. R.*; Rettori, C.*

Photothermal effects in plasmonic nanoparticles can be used to locally modify temperature-sensitive materials. Polylactic acid (PLA) is a thermoplastic biodegradable polymer with a glass transition temperature around 60 degrees C that has been popularized as a feedstock material for 3D printing. Here, we extend its use to produce thin PLA films that can be modified at the microscopic level when covered with gold nanostars (AuNSs). The heat dissipation generated when exciting the plasmon resonance of AuNSs, under exposure to 976 nm focused laser light, produces an increase in the local temperature of more than 100 degrees C. When the temperature surpasses the glass transition of the base PLA layer, AuNSs get attached to the polymer surface. The following dissolution of the unexposed material in acetone bath permits the precise control of the engraving process at the microscale. Furthermore, Er3+ doped upconverting nanoparticles embedded into the PLA layer can act as optical nanothermometers to probe the local temperature, simultaneously allowing the visualization of the laser spot. A computer numerical control (CNC) system was developed to drive the laser writing beam and transfer 2D patterns, opening up the thermoplasmonic maskless lithography technique.Suitable for rigid and flexible substrates coated with PLA, the methods and materials developed here were applied to produce patterned substrates for surface enhanced Raman spectroscopy and luminescent optical encoding for anticounterfeiting technologies.

ACS APPLIED NANO MATERIALS 2[11], 6889-6897, 2019. DOI: 10.1021/acsanm.9b01355

[P494-2019] "Using thermochemical treatment for facilitating apatite formation on Ti-Nb-Sn alloys"

Rezende, A. C. S. A.; Wang, J.; Li, Y.; Gomes Carvalho, A. M.; Souza, M. V. de B.; Santos, S. Jr.; Martins, A.; Costa, A. M. da S.; Cremasco, A.; **Landers, R.***; Machado, D.; Pancotti, A.

Titanium alloys are promising candidates for biomedical applications, and alloys based on the Ti-rich side of Ti-Nb-Sn system have presented material properties deserved for orthopedic implant applications. However, to our knowledge, the structural studies related to surface of these alloys are limited. Ti-18Nb-11Sn and Ti-35Nb-4Sn alloys were synthesized, and the influence of thermochemical treatment on the bioactivity was investigated. The alloys were synthesized by arc melting furnace and then were submitted to thermochemical treatment. X-ray diffraction and scanning electron micrograph analysis showed high crystallinity and maintenance of microstructure of the both alloys before and after thermochemical treatment. The results indicated that the Ti-18Nb-11Sn alloy was not demonstrated to be bioactive, while the Ti-35Nb-4Sn alloy slightly presented bioactivity, which increased after the thermochemical treatment. Meanwhile, the Ti-18Nb-11Sn alloy presented a low hardness value, making it not compatible with biomedical applications. However, the Ti-35Nb-4Sn alloy presented an acceptable hardness value for biomedical applications. We believe that the results reported herein suggest that the Ti-35Nb-4Sn alloy may be attractive for designing biomedical devices with improved performances toward the adhesion of apatite.

JOURNAL OF MATERIALS SCIENCE 55[10], 4395-4407, 2019. DOI: 10.1007/s10853-019-04281-2

[P495-2019] "X-ray Photoelectron Fingerprints of High-Valence Ruthenium-Oxo Complexes along the Oxidation Reaction Pathway in an Aqueous Environment"

Silva, J. L.; Unger, I.; Matias, T. A.; Franco, L. R.; Damas, G.; Costa, L. T.; Toledo, K. C. F.; Rocha, T. C. R.; **de Brito, A. N.***; Saak, C.-M.; Coutinho, K.; Araki, K.; Bjorneholm, O.; Brena, B.; Araujo, C. M.

Recent advances in operando-synchrotron-based X-ray techniques are making it possible to address fundamental questions related to complex proton-coupled electron transfer reactions, for instance, the electrocatalytic water splitting process. However, it is still a grand challenge to assess the ability of the different techniques to characterize the relevant intermediates, with minimal interference on the reaction mechanism. To this end, we have developed a novel methodology employing X-ray photoelectron spectroscopy (XPS) in connection with the liquid-jet approach to probe the electrochemical properties of a model electrocatalyst, [Ru-II(bpy)(2)(py)-(OH2)](2+), in an aqueous environment. There is a unique fingerprint of the extremely important higher-valence ruthenium-oxo species in the XPS spectra along the oxidation reaction pathway. Furthermore, a sequential method combining quantum mechanics and molecular mechanics is used to illuminate the underlying physical chemistry of such systems. This study provides the basis for the future development of in-operando XPS techniques for water oxidation reactions.

JOURNAL OF PHYSICAL CHEMISTRY LETTERS 10[24], 7636-7643, 2019. DOI: 10.1021/acs.jpclett.9b02756

Eventos publicados 2019

[P496-2019] "Classification Performance of SSVEP Brain--Computer Interfaces Based on Functional Connectivity"

Rodrigues, P. G.; Silva Junior, J. I.; Costa, T. B. S.; Attux, R.; **Castellano, G.*;** Soriano, D. C.

Brain connectivity analysis via complex networks has been widely applied to elucidate functional aspects related to brain diseases, such as Alzheimer and Parkinson, and, more recently, to investigations concerning the functional organization of brain regions under motor imagery in brain computer interfaces (BCIs). Therefore, this work seeks to investigate the classification performance of steady-state visually evoked potential (SSVEP) brain-computer interfaces based on functional connectivity. Two different approaches were chosen for extracting functional connectivity and estimating the adjacency matrix from SSVEP-EEG signals: classical Pearson correlation and a new proposal based on Space-Time recurrence counting. These strategies were followed by graph feature evaluation (clustering coefficient, degree, betweenness and eigenvalue centralities), feature selection via Davies-Bouldin index and classification using a least squares classifier for 15 subjects in a 4-command SSVEP-BCI system. For comparison, we also employed a classical spectral feature extraction approach based on the fast Fourier transform (FFT). It was observed that it is possible to separate the classes with a mean accuracy of 0.56 for Pearson and 0.61 for the STR framework, with the clustering coefficient and the eigenvector centrality being the best attributes for these scenarios, respectively. Nonetheless, classical FFT-based feature extraction obtained the best decoding performance.

XXVI BRAZILIAN CONGRESS ON BIOMEDICAL ENGINEERING, CBEB 2018, VOL. 2, IFMBE Proceedings 70[2], 115-120, 2019. DOI: 10.1007/978-981-13-2517-5_18

[P497-2019] "Dissecting the region around IceCube--170922A: the blazar TXS 0506+056 as the first cosmic neutrino source"

Glauch, T.; Padovani, P.; Giommi, P.; Resconi, E.; **Arsioli, B.***; Sahakyan, N.; Huber, M.; Spiering, C. [ed.]

On MJD 58018 the IceCube neutrino observatory detected a highly energetic, well-reconstructed neutrino, IceCube-170922A, at a distance of 0.1 degrees to a gamma-ray flaring blazar, TXS 0506+056. Follow-up searches in archival data additionally revealed a larger flare of neutrinos from the same direction. In order to complete the picture we present here a full multi-wavelength study of the region around IceCube-170922A. While we identify also other non-thermal counterpart candidates, we show that all the evidence points to TXS 0506+056 as the dominant neutrino emitter. Additionally, an analysis of all the available Fermi-LAT data indicates a hard spectrum/low flux of TXS 0506+056 during the neutrino flare in contrast to a soft spectrum/high flux at the arrival time of IceCube-170922A. Putting all the pieces together we conclude that the SED of TXS 0506+056 can be energetically reconnected for both neutrino observations.

8th Conference on Very Large Volume Neutrino Telescopes (VLVnT). Dubna, RUSSIA. OCT 02-04, 2018.

VERY LARGE VOLUME NEUTRINO TELESCOPES (VLVNT-2018). EPJ Web of Conferences 207, UNSP 02003, 2019. DOI: 10.1051/epjconf/201920702003

[P498-2019] "EEG Functional Connectivity Patterns Over the Course of Neurofeedback Attention Training for Healthy Subjects: A Pilot Study"

Stefano Filho, C. A.; de Menezes, L. T.; Pigatto, J. O. F.; **Castellano, G.***

Neurofeedback (NFB) training has been applied as a complementary or alternative treatment to several neurological conditions, such as attention deficit and hyperactivity, epilepsy, anxiety, amongst others. However, the technique has yielded controversial findings, mainly due to non-standardized and uncontrolled studies. Moreover, research indicating apparent benefits of NFB training often do not investigate how the observed behavior changes relate to subjacent neural mechanisms. In this study, our aim was to verify whether measures of functional connectivity (FC) changed with the NFB training sessions, and if such variations could be related to the subject's subjective perception of their attention capacity. We analyzed electroencephalography (EEG) data during the resting state (RS) condition for three healthy subjects over 10 NFB sessions and assumed that there are individual, specific sets of FC links that remain for, at least, a certain fraction r of the total RS recording. By setting r = 0.7, we computed the number of these frequent links over the NFB sessions. Overall, we found that pre and post-NFB training RS recordings tend to present distinct patterns, and that there can be specific increasing or decreasing trends for each subject. On the other hand, no correlations were found between the FC results and the subjects' answers regarding their subjective perception of attention. Inclusion of more subjects and other experimental groups, such as control and/or false-NFB, will be performed next to provide more certain insights.

XXVI BRAZILIAN CONGRESS ON BIOMEDICAL ENGINEERING, CBEB 2018, VOL. 2, IFMBE Proceedings 70[2], 167-173, 2019. DOI: 10.1007/978-981-13-2517-5_26

Correções 2019

[Co002-2019] "Insight into particle production mechanisms via angular correlations of identified particles in pp collisions at root s = 7 TeV (vol 77, 569, 2017)"

Acharya, S.; Adam, J.; Adamova, D.; **Albuquerque, D. S. D.*; Chinellato, D. D.*; De Souza, D.*; Takahashi, J.***; et. al.; ALICE Collaboration

EUROPEAN PHYSICAL JOURNAL C 79[12], 998, 2019. DOI: 10.1140/epjc/s10052-019-7398-8

Artigos publicados 2020

[P001-2020] "a-C:H films produced by PECVD technique onto substrate of Ti6Al4V alloy: Chemical and biological responses"

Euridice, W.A.; Leite, N.B.; Gelamo, R.V.; Buranello, P.A.D.; da Silva, M.V.; de Oliveira, C.J.F.; Lopez, R.F.V.; Lemos, C.N.; **de Siervo, A.***; Moreto, J.A.

This work aims to investigate the chemical and biological responses of a-C:H films produced by PECVD technique onto substrate of Ti6Al4V alloy. The films produced were characterized morphologically and structurally by optical microscope (OM), SEM, AFM, EDX, FTIR Raman Spectroscopy (RS) and XPS. Afterwards, biocompatibility and cytotoxicity tests on osteoblastic cells and/or Human Peripheral Blood Mononuclear Cells (PBMCs) were performed on the Ti6Al4V alloy with coated and uncoated a-C:H film. The I-D/I-G ratio about 0.71 suggests a hydrogenated amorphous carbon film (a-C:H). The deconvoluted XPS spectra of C 1s peaks disclose the presence of three main components: Cl associated to C=C bonds in one sp(2) hybridization as well as C2 associated to sp(3) hybridization. The impedance results showed that a-C:H film acts as a protective barrier against the corrosion process. Regardless of the cell population, when the total apoptosis of osteoblastic cells or PBMCs was evaluated, only cells cultured on the alloy without a-C:H had significant induction of the apoptotic process. Moreover, only PBMCs cultured on the alloy without a-C:H had significant induction of inflammatory and anti-inflammatory cytokines that characterize immune activation.

APPLIED SURFACE SCIENCE 503, UNSP 144084, 2020. DOI: 10.1016/j.apsusc.2019.144084

[P002-2020] "Adsorption of Gold Ions onto Sericin and Alginate Particles Chemically Crosslinked by Proanthocyanidins: a Complete Fixed-Bed Column Study"

Santos, N.T.D.; **Landers, R.***; da Silva, M.G.C.; Vieira, M.G.A.

In this study, we evaluated the adsorption of gold ions onto sericin and alginate particles chemically crosslinked by proanthocyanidins (SAPAS) in a fixed-bed column aiming at establishing a new profitable application for sericin. The effects of the feed flow rate and the gold inlet concentration on the breakthrough curve behavior were investigated. A breakthrough time of more than four and a half days with a removal efficiency of 98.39% (maximum removal capacity of 57.91 mg/g) was obtained for the breakthrough curve performed at the lowest feed flow rate and the lowest gold inlet concentration (0.4 mL/min and 53.18 mg/L, respectively). All breakthrough curves were best described by the Yan et al. model. The two adsorption/desorption cycles performed using thiourea (0.5 M)/hydrochloric acid (0.5 M) as the eluent resulted in low values of gold recovery percentage (recoveries of 24.98 and 22.6% for the first and second cycle, respectively), which indicated predominance of chemical interactions between SAPAS and gold. On the other hand, an efficient recovery of gold (89.00%) was achieved from the association between the adsorption and incineration processes. X-ray photoelectron spectroscopy and X-ray diffraction analyses indicated that gold was reduced from Au(III) to metallic gold during the adsorption process.

INDUSTRIAL & ENGINEERING CHEMISTRY RESEARCH 59, 1, 318-328, 2020. DOI: 10.1021/acs.iecr.9b04914

[P-003-2020] "An assessment of biomedical CoCrMo alloy fabricated by direct metal laser sintering technique for implant applications"

Girao, D.D.; Beres, M.; Jardini, A.L.; Maciel, R.; Silva, C.C.; **de Siervo, A.***; de Abreu, H.F.G.; Araujo, W.S.

CoCrMo alloys have been used for several decades in implantable devices due to their favourable mechanical properties, low wear rate in addition to good biocompatibility and high corrosion resistance. These alloys are conventionally produced via casting and/or forging route, however additive manufacturing techniques being recently employed in their fabrication. In this work, CoCrMo samples were produced by direct metal laser sintering additive manufacturing process. The microstructure and surface composition were examined employing scanning electron microscopy, X-ray diffraction and X-ray photoelectron spectroscopy (XPS). The corrosion resistance was measured in 0.14 M sodium chloride solution and in phosphate buffered solution (PBS) both with and without addition of albumin at pH 7.4 and 37 degrees C. For this, potentiodynamic tests in addition to electrochemical impedance spectroscopy were employed. The studied CoCrMo alloy exhibits a good corrosion resistance in solutions tested being the highest in PBS solution without albumin addition. The XPS analysis showed that the passive film composition and its thickness are not modified by the adsorbed layer. Microstructural analysis revealed occurrence of strain-induced martensitic transformation.

MATERIALS SCIENCE & ENGINEERING C-MATERIALS FOR BIOLOGICAL APPLICATIONS 107, 110305, 2020. DOI: 10.1016/j.msec.2019.110305

[P004-2020] "Combined search for supersymmetry with photons in proton-proton collisions at root s=13 TeV"

Sirunyan, A. M.; Tumasyan, A.; Adam, W.; **Chinellato, J. A.*; Tonelli Manganote, E. J.***; et al. CMS Collaboration

A combination of four searches for new physics involving signatures with at least one photon and large missing transverse momentum, motivated by generalized models of gauge-mediated supersymmetry (SUSY) breaking, is presented. All searches make use of proton-proton collision data at root s = 13 TeV, which were recorded with the CMS detector at the LHC in 2016, and correspond to an integrated luminosity of 35.9 fb(-1). Signatures with at least one photon and large missing transverse momentum are categorized into events with two isolated photons, events with a lepton and a photon, events with additional jets, and events with at least one high-energy photon. No excess of events is observed beyond expectations from standard model processes, and limits are set in the context of gauge-mediated SUSY. Compared to the individual searches, the combination extends the sensitivity to gauge-mediated SUSY in both electroweak and strong production scenarios by up to 100GeV in neutralino and chargino masses, and yields the first CMS result combining various SUSY searches in events with photons at root s = 13 TeV.

PHYSICS LETTERS B 801, 135183, 2020. DOI: 10.1016/j.physletb.2019.135183

[P005-2020] "Dynamic Local Strain in Graphene Generated by Surface Acoustic Waves"

Fandan, R.; Pedros, J.; Hernandez-Minguez, A.; **Iikawa, F.***; Santos, P.V.; Bosca, A.; Calle, F.

We experimentally demonstrate that the Raman-active optical phonon modes of single-layer graphene can be modulated by the dynamic local strain created by surface acoustic waves (SAWs). In particular, the dynamic strain field of the SAW is shown to induce a Raman scattering intensity variation as large as 15% and a phonon frequency shift of up to 10 cm(-1) for the G band, for instance, for an effective hydrostatic strain of 0.24% generated in single-layer graphene atop a LiNbO3 piezoelectric substrate with a SAW resonator operating at a frequency of similar to 400 MHz. Thus, we demonstrate that SAWs are powerful tools for modulating the optical and vibrational properties of supported graphene by means of the high-frequency localized deformations tailored by the acoustic transducers, which can also be extended to other 2D systems.

NANO LETTERS 20, 1, 402-409, 2020. DOI: 10.1021/acs.nanolett.9b04085

[P006-2020] "Energy barriers for collapsing large-diameter carbon nanotubes"

Grande, R. R. Del; **Fonseca, A. F.***; Capaz, R. B.

Single-wall carbon nanotubes (SWNTs) are best known in their hollow cylindrical shapes, but the ground state of large-diameter tubes actually corresponds to a collapsed dumbbell-like structure, where the opposite sides of the nanotube wall are brought in contact and stabilized by van der Waals attraction. For those tubes, the cylindrical shape is metastable and it is interesting to investigate the energy barrier for jumping from one configuration to another. We calculate the energy barrier for SWNT collapse by considering a transition pathway that consists of an initial local deformation that subsequently propagates itself along the SWNT axis. This leads to finite and physically meaningful energy barriers in the limit of infinite nanotubes. Yet, such barriers are surprisingly large (tens of eV) and therefore virtually unsurmountable, which essentially prevents the thermal collapse of a metastable cylindrical at any reasonable temperatures. Moreover, we show that collapse barriers increase counterintuitively with SWNT diameter. Finally, we demonstrate that, despite such huge barriers, SWNTs may collapse relatively easily under external radial forces and we shed light on recent experimental observations of collapsed and cylindrical SWNTs of various diameters.

CARBON 159, 161-165, 2020. DOI: 10.1016/j.carbon.2019.12.030

[P007-2020] "Freestanding and flexible composites of magnetocaloric Gd-5(Si,Ge)(4) microparticles embedded in thermoplastic poly(methyl methacrylate) matrix"

Andrade, V.M.*; Barroca, N.B.; Pires, A.L.; Belo, J.H.; Pereira, A.M.; **Pirota, K.R.***; Araujo, J.P.

The implementation of processed magnetic materials onto thermoplastics can be an approach for practical use of brittle intermetallic materials on device development with the advantage of enlarging the range of applications. In this paper, we present the evaluation on the effect of blending magnetocaloric Gd5Si2.4Ge1.6 3.4 mu m particles with in different weight fractions onto a flexible, transparent and non-magnetic poly(methyl methacrylate) (PMMA). A close to homogeneous grain distribution along the polymer surface were achieved by using a simple solvent casting method for their magnetocaloric properties studies. From XRD analysis, it was found a unit cell volume shrinkage by increasing the powder concentration followed by a reduction on the amount of secondary monoclinic phase as a result of interfacial interactions. As a consequence, a weakening of secondary phases effect on the composite magnetocaloric behavior is observed as a result of the effective hydrostatic pressure from the difference between thermal expansions of matrix and filler.

MATERIALS & DESIGN 186, 108354, 2020. DOI: 10.1016/j.matdes.2019.108354

[P008-2020] "Hydrogenation Dynamics Process of Single--Wall Carbon Nanotube Twisted"

De Sousa, J. M.; Autreto, P. A. S.; **Galvao, D. S.***

In some of the technological applications (electromechanical oscillators and mechanical actuators for artificial muscles, for instance), carbon nanotubes (CNT) are subjected to large deformations. Although this frequently happens in the air, there are only a few studies about the interaction of deformed CNT with the atmosphere and the dynamics of these processes. We have investigated, through fully atomistic reactive molecular dynamics simulations, the process of hydrogenation of highly twisted CNT. Our results show that the effective hydrogenation ratio is directly related to the twist angle values. This could be used to control the rates of gas absorption in CNT.

CHEMICAL PHYSICS LETTERS 739, 136960, 2020. DOI: 10.1016/j.cplett.2019.136960

[P009-2020] "Measurement of the single top quark and antiquark production cross sections in the t channel and their ratio in proton-proton collisions at root s=13 TeV"

Sirunyan, A. M.; Tumasyan, A.; Adam, W.; **Chinellato, J. A.*; Tonelli Manganote, E. J.***; et al. CMS Collaboration

Measurements of the cross sections for the production of single top quarks and antiquarks in the t channel, and their ratio, are presented for proton-proton collisions at a center--of-mass energy of 13 TeV. The data set used was recorded in 2016 by the CMS detector at the LHC and corresponds to an integrated luminosity of 35.9 fb(-1). Events with one muon or electron are selected, and different categories of jet and b jet multiplicity and multivariate discriminators are applied to separate the signal from the background. The cross sections for the t-channel production of single top quarks and antiquarks are measured to be 130 +/- 1(stat) +/- 19(syst) pb and 77 +/- 1(stat) +/- 12(syst) pb, respectively, and their ratio is 1.68 +/- 0.02(stat) +/- 0.05(syst). The results are in agreement with the predictions from the standard model.

PHYSICS LETTERS B 800, 135042, 2020. DOI: 10.1016/j.physletb.2019.135042

[P010-2020] "Mechanical and energy-absorption properties of schwarzites"

Felix, L.C.*; Woellner, C.F.; **Galvao, D.S.***

We investigated through fully atomistic molecular dynamics simulations, the mechanical behavior (compressive and tensile) and energy absorption properties of two families (primitive (P688 and P8bal) and gyroid (G688 and G8bal)) of carbon--based schwarzites. Our results show that all schwarzites can be compressed (with almost total elastic recovery) without fracture to more than 50%, one of them can be even remarkably compressed up to 80%. One of the structures (G8bal) presents negative Poisson's ratio value (auxetic behavior). The crush force efficiency, the stroke efficiency and the specific energy absorption (SEA) values show that schwarzites can be effective energy absorber materials. Although the same level of deformation without fracture observed in the compressive case is not observed for the tensile case, it is still very high (30-40%). The fracture dynamics show extensive structural reconstructions with the formation of linear atomic chains (LACs).

CARBON 157, 670-680, 2020. DOI: 10.1016/j.carbon.2019.10.066

[P011-2020] "Micro-Raman Spectroscopy of Zircon (ZrSiO4) Mineral at Annealing Conditions Usually Applied in Zircon Fission-Track Annealing Dataset"

Dias, A.N.C.; Constantino, C.J.L.; Soares, C.J.; **de Oliveira, S.G.***

Raman analyzes were performed on zircon from a syenite located in the Pocos de Caldas Complex, Brazil, with a fission-track (FT) zircon age of 81.4 +/- 6.8 Ma. Three isochronous heating (1, 10 and 100 hours) of zircon grains were subjected to temperatures between 300 and 750 degrees C. These temperature and times are usually applied to obtain zircon Fission-Track annealing dataset. For each time-temperature conditions, Raman spectra analyses were accomplished. The results show variations in the intensity and FWHM (full width at half maximum) in the main band (1007 cm(-1)-Si-O stretching mode), and a singular change in the peaks from 356 to 439 cm(-1) (Si-O bending mode); and from 202 to 224 cm(-1) (external modes). These changes were interpreted as spectral polarization-dependence related to common crystallinity increases due to the annealing radiation damages and that the thermal treatments do not interfere on the stability of zircon lattice.

JOURNAL OF NANOSCIENCE AND NANOTECHNOLOGY 20, 3, 1884-1891, 2020. DOI: 10.1166/jnn.2020.17172

[P012-2020] "Monte Carlo simulation of hybrid pixel detectors"

Magalhaes, D. P.; **Tomal, A.***

Semiconductor sensors are extensively used for X-ray detection, both for spectroscopy and 2D imaging. In this work, the Monte Carlo code PENELOPE v. 2014 with the PenEasy v. 2015 extension was applied for simulating a Medipix3RX detector, including the sensor and the ASIC layers. The code was modified to include the charge dispersion effect modelling at the Pixelated Imaging Detector tally, and validated by investigating the influence of the electric field, incident energy, beam position, pixel size and also by determining the Modulation Transfer Function. The results were compared to experimental data and presented a very good agreement. The Monte Carlo simulation can be used to investigate the detector response and its influence on measured data, such as spatial resolution and X-ray spectra distortion. Besides, the simulation can be applied to determine the energy deposition in each layer of the detector, useful for detection efficiency characterization or radiation damage studies.

RADIATION PHYSICS AND CHEMISTRY 167, 108296, 2020. DOI: 10.1016/j.radphyschem.2019.04.046

14th International Symposium on Radiation Physics (ISRP); Natl Univ Cordoba, Cordoba, ARGENTINA. OCT 07-11, 2018.

[P013-2020] "Multiplicity dependence of light (anti-)nuclei production in p-Pb collisions at root s(NN)=5.02 TeV"

Acharya, S.; Adamova, D.; Adhya, S. P.; **Albuquerque, D. S. D.*; Chinellato, D. D.*; De Souza, R. D.*; Takahashi, J.***; et al. ALICE Collaboration

The measurement of the deuteron and anti-deuteron production in the rapidity range -1 < y < 0 as a function of transverse momentum and event multiplicity in p-Pb collisions at root s(NN) = 5.02 TeV is presented. (Anti-)deuterons are identified via their specific energy loss dE/dx and via their time-of-flight. Their production in p-Pb collisions is compared to pp and Pb-Pb collisions and is discussed within the context of thermal and coalescence models. The ratio of integrated yields of deuterons to protons (d/p) shows a significant increase as a function of the charged-particle multiplicity of the event starting from values similar to those observed in pp collisions at low multiplicities and approaching those observed in Pb-Pb collisions at high multiplicities. The mean transverse particle momenta are extracted from the deuteron spectra and the values are similar to those obtained for p and Lambda particles. Thus, deuteron spectra do not follow mass ordering. This behaviour is in contrast to the trend observed for non-composite particles in p-Pb collisions. In addition, the production of the rare He-3 and (3)(He) over bar nuclei has been studied. The spectrum corresponding to all non-single diffractive p-Pb collisions is obtained in the rapidity window -1 < y < 0 and the p(T)-integrated yield dN/dy is extracted. It is found that the yields of protons, deuterons, and He-3, normalised by the spin degeneracy factor, follow an exponential decrease with mass number.

PHYSICS LETTERS B 800, 135043, 2020. DOI: 10.1016/j.physletb.2019.135043

[P014-2020] "Observation of nuclear modifications in W-+/- boson production in pPb collisions at root s(NN)=8.16 TeV"

Sirunyan, A. M.; Tumasyan, A.; Adam, W.; **Chinellato, J. A.*; Tonelli Manganote, E. J.***; et al. CMS Collaboration

The production of W-+/- bosons is studied in proton-lead (pPb) collisions at a nucleon-nucleon centre-of-mass energy of root s(NN) = 8.16 TeV. Measurements are performed in the W-+/- -> mu(+/-)nu(mu) channel using a data sample corresponding to an integrated luminosity of 173.4 +/- 6.1 nb(-1), collected by the CMS Collaboration at the LHC. The number of positively and negatively charged W bosons is determined separately in the muon pseudorapidity region in the laboratory frame vertical bar eta(mu)(lab)vertical bar < 2.4 and transverse momentum p(T) (mu) > 25 GeV/c. The W-+/- boson differential cross sections, muon charge asymmetry, and the ratios of W-+/- boson yields for the proton-going over the Pb-going beam directions are reported as a function of the muon pseudorapidity in the nucleon-nucleon centre-of-mass frame. The measurements are compared to the predictions from theoretical calculations based on parton distribution functions (PDFs) at next-to-leading-order. The results favour PDF calculations that include nuclear modifications and provide constraints on the nuclear PDF global fits.

PHYSICS LETTERS B 800, 135048, 2020. DOI: 10.1016/j.physletb.2019.135048

[P015-2020] "Raman scattering from one and two magnons in magnetoelectric LiNiPO4"

Rigitano, D.*; Vaknin, D.; **Barberis, G. E.*; Granado, E.***

Polarized Raman scattering in magnetoelectric LiNiPO4 shows a sharp resonant peak at 37 cm(-1) in the magnetically ordered phase, originating from a one-magnon excitation of Ni2+ S = 1 localized moments at the zone center. Also, a broad component with maximum intensity at similar to 65 cm(-1) is observed and successfully modeled in terms of light scattering from two--magnon excitations within the framework of the Fleury-Loudon theory using five relevant exchange parameters, providing an independent experimental confirmation of their values previously obtained with inelastic neutron scattering data in this material. An additional peak at 58 cm(-1), already reported in previous works, shows no detectable Zeeman splitting for magnetic fields up to 6 T along the crystallographic a and c directions, excluding one-magnon scattering as a possible assignment for this peak. The possible nature of this excitation is discussed.

PHYSICAL REVIEW B 101, 2, 024417, 2020. DOI: 10.1103/PhysRevB.101.024417

[P016-2020] "Search for light pseudoscalar boson pairs produced from decays of the 125 GeV Higgs boson in final states with two muons and two nearby tracks in pp collisions at root s d=13TeV"

Sirunyan, A. M.; Tumasyan, A.; Adam, W.; **Chinellato, J. A.*; Tonelli Manganote, E. J.***; et al. CMS Collaboration

A search is presented for pairs of light pseudoscalar bosons, in the mass range from 4 to 15 GeV, produced from decays of the 125 GeV Higgs boson. The decay modes considered are final states that arise when one of the pseudoscalars decays to a pair of tau leptons, and the other one either into a pair of tau leptons or muons. The search is based on proton-proton collisions collected by the CMS experiment in 2016 at a center-of-mass energy of 13 TeV that correspond to an integrated luminosity of 35.9 fb(-1). The 2 mu 2 tau and 4 tau channels are used in combination to constrain the product of the Higgs boson production cross section and the branching fraction into 4 tau final state, sigma beta, exploiting the linear dependence of the fermionic coupling strength of pseudoscalar bosons on the fermion mass. No significant excess is observed beyond the expectation from the standard model. The observed and expected upper limits at 95% confidence level on sigma beta, relative to the standard model Higgs boson production cross section, are set respectively between 0.022 and 0.23 and between 0.027 and 0.19 in the mass range probed by the analysis.

PHYSICS LETTERS B 800, 135087, 2020. DOI: 10.1016/j.physletb.2019.135087

Correções 2020

[Co001-2020] "Radiation damage impact on hybrid-pixel detectors data (Reprinted from Radiation Physics and Chemistry, vol 160, pg 63-67, 2019)"

Magalhaes, D. P.; **Rinkel, J.*; Tomal, A.***

This work aimed to quantify the influence of the deposited dose at the hybrid detector ASIC on the resulting image quality. Low (932 +/- 4 Gy) and high (6310 +/- 24 Gy) dose experiments were performed by irradiating a Medipix3RX single chip detector with the polychromatic beam from the Brazilian Synchrotron X-ray Imaging beamline. It was possible to evaluate subtle effects by using a noise component model based on estimating the quantum, electronic and structural noise contributions. Visible effects were quantified by analyzing the evolution of the histogram of the pixel counts at the irradiated area. The dose threshold for subtle damages was 388 +/- 3 Gy deposited in the gate oxide and shallow trench isolation oxide layers, while visible damages were observed for doses higher than 2635 +/- 15 Gy. A recovery of the damaged pixels with time was noticed and quantified, reaching the half--life time at 1.84 +/- 0.02 h after irradiation. These results encourage periodical maintenance procedures, for example through a new equalization matrix generation, which proved to be a possible tool for recovering the detector performance.

RADIATION PHYSICS AND CHEMISTRY 167, 108555, 2020. DOI: 10.1016/j.radphyschem.2019.108555

***Autores da comunidade IFGW**
Fonte: Web of Science on-line (WOS)

Defesas de Dissertações do IFGW

[D001-2020] "Análise de dados de Espectroscopia por Ressonância Magnética utilizando Aprendizado de Máquina na tentativa de auxiliar na predição de farmacorresistência de pacientes de Epilepsia do Lobo Temporal Mesial"
Aluno: Augusto José Peterlervitz
Orientador: Profa. Dra. Gabriela Castellano
Data: 18/02/2020

[D002-2020] "Termodinâmica e Classicalidade"
Aluno: Alexssandre de Oliveira Junior
Orientador: Prof. Dr. Marcos Cesar de Oliveira
Data: 19/02/2020

Defesas de Teses do IFGW

[T001-2020] "Translação de um sistema de óptica de difusão para monitoramento de pacientes neurocríticos"
Aluno: Rodrigo Menezes Forti
Orientador: Prof. Dr. Rickson Coelho Mesquita
Data: 28/01/2020

[T002-2020] "Luminosidade da emissão de neutrinos devido a transição de fase hádrons-quarks no interior de uma estrela de neutrons"
Aluno: Jhon Andersson Rossero Gil
Orientador: Prof. Dr. Ernesto Kemp
Data: 19/02/2020

Fonte: Portal IFGW/Pós-graduação - Agenda de Colóquios, Defesas e Seminários.
Disponível em: http://portal.ifi.unicamp.br/pos-graduacao

***Nestes primeiros meses não há informações sobre Defesas de Dissertações e Teses do PECIM.**

Fique por dentro!

A partir de fevereiro de 2020 o Boletim Abstracta tem um novo endereço web:

<https://econtents.bc.unicamp.br/boletins/index.php/abstracta>

Abstracta

Instituto de Física
Diretor: Prof. Dr. Pascoal José Giglio Pagliuso
Diretora Associada: Profa. Dra. Mônica Alonso Cotta
Universidade Estadual de Campinas - UNICAMP
Cidade Universitária Zeferino Vaz
13083-859 - Campinas - SP - Brasil
e-mail: secdir@ifi.unicamp.br
Fone: +55 19 3521-5300

Publicação

Biblioteca do Instituto de Física Gleb Wataghin
http://portal.ifi.unicamp.br/biblioteca

Diretora Técnica: Sandra Maria Carlos Cartaxo
Coordenadora da Comissão de Biblioteca: Profa. Dra. Arlene Cristina Aguilar

Elaboração:
Maria Graciele Trevisan (Bibliotecária)
Ayres Neri da Cunha Junior (Técnico Administrativo)
contato: infobif@ifi.unicamp.br